Numerical modeling of waste cooking oil biodiesel combustion in a turbulent swirl burner

D. Füzesi*, [1], D. Csemány[1], C.T. Chong[2], V. Józsa[1]

[1]Department of Energy Engineering, Faculty of Mechanical Engineering, BME, 1111 Budapest, Hungary;
fuzesi@energia.bme.hu (D.F.); csemany@energia.bme.hu (D.Cs.); jozsa@energia.bme.hu (V.J.)
[2]China-UK Low Carbon College, Shanghai Jiao Tong University, 201306 Lingang, Shanghai; ctchong@sjtu.edu.cn

Abstract
Liquid fuels are the most valuable for transportation, and this trend seems to live on for the foreseeable decades. Consequently, increasing the share of renewable content is a critical point towards carbon neutrality. The present paper focuses on numerical modeling and comparison of diesel fuel and waste cooking oil (WCO) biodiesel combustion in a novel turbulent swirl burner that offers ultra-low NO_x emissions. The results were validated by flame images and NO_x emission data. The most significant result was the simulation of distributed combustion by robust simulation models.

Introduction

Liquid fuels are the most versatile in terms of logistics and safety, hence, they will dominate the transportation sector for several decades [1]. To reduce our dependence on fossil fuels, biofuels are blended with fossil fuels and sold commercially, e.g., E10 and B7, referring to 10% ethanol in petrol and 7% biodiesel in diesel fuel, respectively. If these biofuels are produced from crops, classified as first-generation biofuels, then food safety emerges [2]. To mitigate this problem, waste-derived fuels can be used from which the conversion of waste cooking oil (WCO) to biodiesel is a highly favorable option since it requires less than 1% energy of the final product [3]. Moreover, this is a second-generation biofuel that means it requires no arable land, not competing with food crops. Even though only a small fraction of our energy needs can be covered by WCO-based fuels, its potential is high enough to exploit this valuable and environmentally friendly resource worldwide. The collection and management of WCO is a social problem [4] that requires both governmental and local support to work socially efficiently.

Fuel properties of WCO-based biodiesel are close to that of the straight vegetable oil biodiesels; there is no notable difference in their molecular structure [5]. The actual composition highly depends on the feedstock [6]. However, properties affecting spray formation and volatility characteristics are rather similar [7].

To meet the pollutant emission requirements, steady-operating combustion systems either use rich burn-quick quench-lean burn combustion concept or lean premixed burners [8]. To reduce principally the NO_X emission even further, MILD combustion is currently under research [9]. The required flue gas or inert gas dilution [10] is not an option in several practical systems, e.g., gas turbines. For this purpose, the Mixture Temperature-Controlled (MTC) combustion was recently introduced [11]. To understand the operation of this concept better, the present study aims to numerically investigate the associated distributed combustion achieved by using ambient air as the oxidizer.

The liquid fuel combustion simulations were performed in Ansys Fluent 2020 R1 software environment. Due to the excessive number of species and the real-scale computational domain with a multiphase flow, a thermochemical probability density function-based (PDF) combustion model was used. In the case of premixed combustion, a partially premixed model is more appropriate than the non-premixed model [12]. To simplify atomization, it was modeled in a Lagrangian domain [13,14]. The Extended Coherent Flame combustion model was used in an Eulerian-Lagrangian domain, using a thermochemical probability density function-based lookup table [15]. WCO and diesel fuel combustion, as reference fuel, were simulated by RANS model, similar to the work of Kuti et al. [14]. 2D biodiesel blend combustion simulations were performed in ref. [16], however, in the case of swirl combustion, a 3D model is inevitable to properly estimate the governing flow structures in a reactive environment.

The goal of the present study is principally the simulation of distributed combustion of diesel and WCO biodiesel fuels in 3D, using robust modeling techniques. The models were validated against flame images and pollutant emission data.

Materials and methods

The swirl burner geometry with 45° vanes is shown in Fig. 1. Tip and hub diameters were 40 and 21 mm. The flow field of the swirl vanes was analyzed separately for computational reasons. The hybrid hexa-tetrahedral mesh created in Ansys ICEM CFD can be seen in Fig. 2 a), which consists of 705500 cells. The resulting pressure drop, tangential, and radial velocity profiles were transferred to the entire combustion system model, shown in Fig. 3. Here the polyhedral mesh was created in Ansys Fluent Meshing. The mesh sensitivity analysis showed that 389000 cells are appropriate for the combustion simulations. An interior face was added to represent the swirl vanes as a fan boundary condition. An additional 200 mm combustion chamber length was

* Corresponding author: fuzesi@energia.bme.hu

added to mitigate the problems associated with reverse flow.

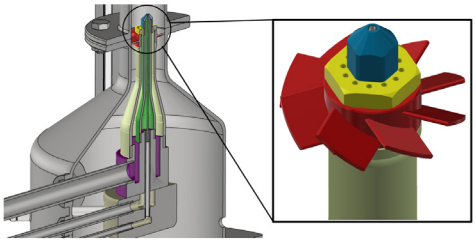

Fig. 1. CAD geometry of the investigated burner. The airblast atomizer is blue

The boundary conditions are indicated in Figs. 2 b) and c). The turbulence model was *k-ω* SST. For the outer walls, convection boundary condition was used with 20 °C ambient temperature and heat transfer coefficient of 9.77 W/m^{2}K, which was 8.39 W/m^{2}K in the case of the mixing tube, based on ref. [17]. Thermal radiation was considered through the Discrete Ordinates model. The emissivity of the stainless steel outer walls was 0.5 [18].

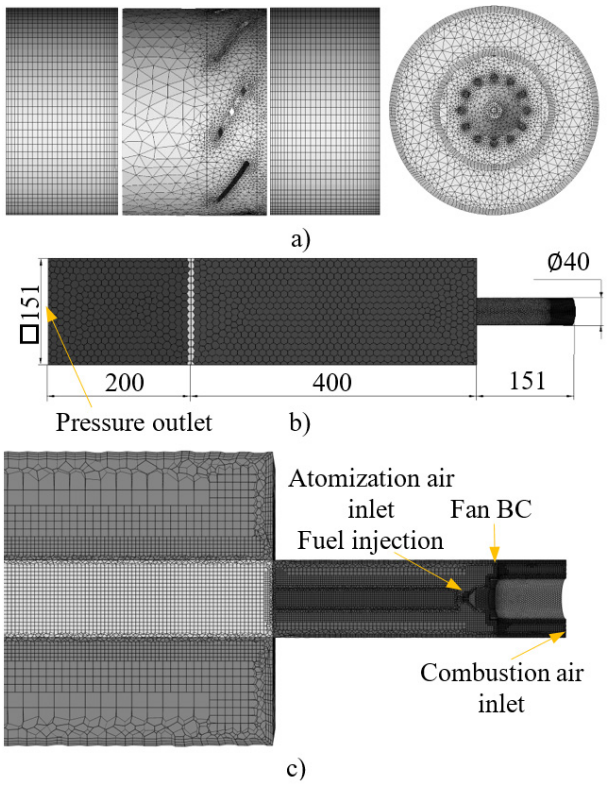

Fig. 2. a) Tetrahedral mesh of the burner, b) polyhedral surface mesh of the whole computational domain, and c) polyhedral volume mesh of the combustion chamber, mixing tube, and atomizer nozzle.

The atomization process was modeled by the airblast atomizer model in a Lagrangian frame using the Discrete Phase Model. The secondary breakup was considered by the Kelvin-Helmholtz Rayleigh-Taylor model. The spray half cone angle was defined as 11° [19], and the diameter of the nozzle was 0.9 mm. NO_x emission was estimated by reaction rate of thermal NO_x formation from the calculated instantaneous N_2, O_2, and O concentration with PDF-based turbulence-chemistry interaction.

The investigated air-to-fuel equivalence ratio (λ) and atomizing gauge pressure (p_a) values are shown in Table 1. Table 2 contains the lower heating values (LHV) and stoichiometric air-to-fuel ratio (AFR) of WCO and diesel fuel (D), which was modeled as n-dodecane, similar to ref. [20]. The thermal power was uniformly 13.3 kW. The combustion air inlet temperature was 200 °C. After reaching convergence, the values were averaged by iteration steps.

Table 1. Investigated air-to-fuel equivalence ratio and atomization gauge pressure.

Case	λ [-]	p_a [bar]
1	1.167	0.3
2	1.5	0.3
3	1.75	0.75
4	1.75	0.9

Table 2. Fuel properties.

	diesel (n-$C_{12}H_{26}$)	**WCO**
LHV [MJ/kg]	43	37.2
AFR [kg/kg]	14.4	12.5

WCO was considered as a quasi one-component fuel, and the properties were averaged from the available FAME composition. Table 3 contains the sources of reference data and computational methods for the required material properties. Some of them are constant, e.g., normal boiling point, T_{bn}, and latent heat of vaporization at the normal boiling point, L_{Tbn}. Others are temperature-dependent and correspond to 1 bar atmospheric pressure. Properties of n-dodecane are gathered mainly from the National Institute of Standards and Technology (NIST) [21]. Where no reference data was available for the evaluated temperature range and also for the material properties of WCO, estimation methods were used to get the needed properties. These techniques were tested for n-alkanes and methyl esters and provided sufficient accuracy. T_{bn} of n-dodecane is 489.3 K, which is close to the initial boiling point of the measured diesel fuel sample with a value of 502.5 K. T_{bn} of WCO was acquired from ASTM D86 distillation curve (DC) data. Since the temperature difference between the initial boiling point and the temperature corresponding to 95% distilled volume fraction of the sample is 50 K, the integral mean value of the DC was used, which is 635.9 K. L_{Tbn} of $C_{12}H_{26}$ is 256 kJ/kg, while for WCO, the calculated value of methyl oleate, 225 kJ/kg was used since its share in the total FAME composition is 46.96 m/m% for the investigated biodiesel sample. Note that the vapor pressure curve, p_{vs}, for WCO was also determined for methyl oleate with the Antoine equation. A polynomial fit was performed for each temperature-dependent property on the investigated temperature range and implemented in the model to facilitate calculations. Liquid-phase density (ρ_l), specific heat capacity ($c_{p,l}$), dynamic viscosity (μ_l), and surface tension (σ) were

available from 260 K up to T_{bn} from NIST or by calculation methods. The temperature interval for vapor-phase specific heat capacity ($c_{p,v}$), dynamic viscosity (μ_v), thermal conductivity (k_v), and mutual diffusion coefficient of vapor and air ($D_{v,a}$) ranged from 280 K to 2000 K. Appropriate mixing rules for the temperature-dependent properties were applied, e.g., mass-averaged and molar-averaged values, for WCO according to the FAME composition.

Table 3. Overview of the reference data and computational methods for the relevant material properties.

	diesel (n-$C_{12}H_{26}$)	WCO
T_{bn}	NIST	DC data
L_{Tbn}	NIST	Riedel [22]*
ρ_l	NIST	Elbro [23]
$c_{p,l}$	NIST	Ruzicka [24]
μ_l	NIST	Ramírez [25]
σ	Brock [26]	
$c_{p,v}$	Joback [27,28]	
μ_v	Lucas [29]	
k_v	Modified Eucken method [30]	
$D_{v,a}$	Fuller [31,32]	
p_v	NIST	Antoine equation [33]*

* property corresponding to methyl oleate.

Results and discussion

The CFD model was validated against flame images of D combustion, shown in Fig. 3. The recording settings of all images were identical. However, images of cases 3 and 4 were dark, hence, intensified later for better visibility. Below the flame shapes, the simulated temperature contours are shown for qualitative comparison. The following flame shapes were observed. Case D1 – straight flame, case D2 – V, case D3, and D4 – distributed flame. Table 4 shows the mass-weighted average of NO_x emission by CFD and the measured values [11] at the combustion chamber outlet. The difference in magnitude is attributed to the lower temperatures in reality and the higher loss. Nevertheless, the qualitative match is fair. A better result could be achieved by using a detailed reaction kinetic model and tuning the NOx model. None of them was a goal of the present study to remain simple and consistent.

Table 4. NO_x emission at the outlet at 15% O_2 in the case of diesel fuel combustion.

Case	Simulated [ppm]	Measured [ppm]
1	165.4	31.3
2	50.1	12.4
3	3.7	2.5
4	0.3	2

Combustion of WCO is presented in Fig. 4, showing the temperature distribution. Cases WCO1 and WCO2 are relatively similar, and the fuel surrogate did not reproduce the V-shaped flame. Also, the transition to distributed combustion was not as flawless as in the case of D. Nevertheless, the notable drop in overall temperature is evident for the WCO3 and WCO4 cases. However, the simulated temperature is higher than that in the case of D combustion.

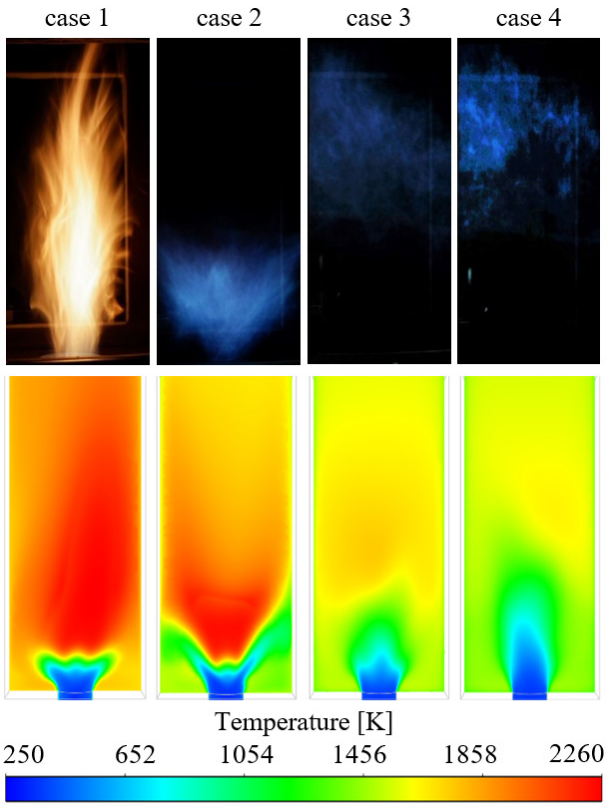

Fig. 3. Flame images (top row) and temperature distribution (bottom row) of D combustion.

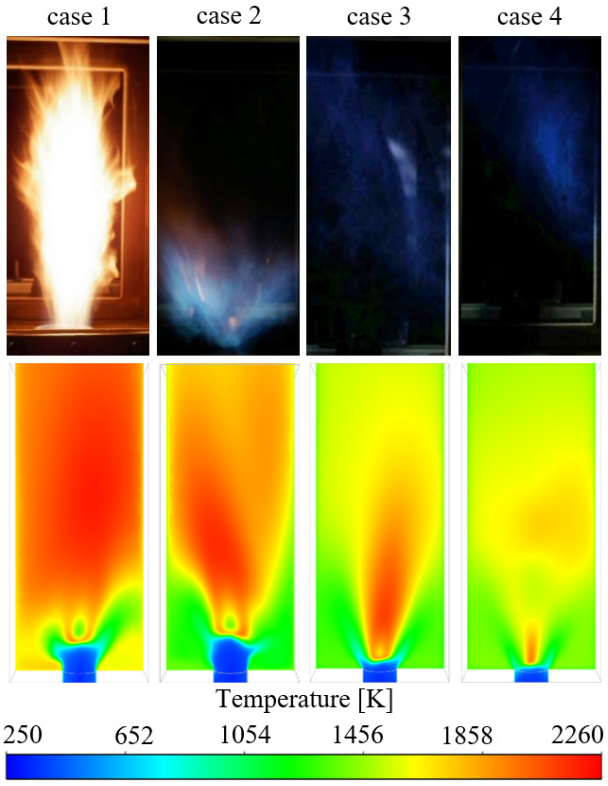

Fig. 4. Flame images (top row) and temperature distribution (bottom row) of WCO combustion.

Figure 5 indicates the OH* distribution representing the heat release of the flame. Following the previous trends in the temperature field, the intensity values are higher for WCO combustion.

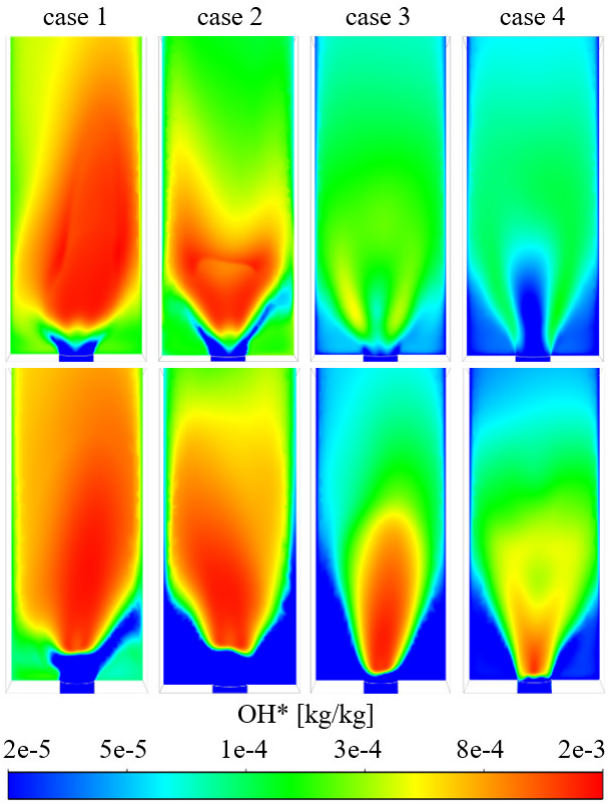

Fig. 5. OH* distribution of D (top row) and WCO combustion (bottom row). Note the log scale.

The comparison of fluid dynamical characteristics is shown in Figs. 6–9. Figure 6 presents the flow field by vector plots to show the swirling flow characteristics. Outer Recirculation Zones (ORZ) are marked with red ellipses, and Inner Recirculation Zones (IRZ) are marked with black ellipses. ORZs were developed in each case, while IRZ was only identified for D2, indicating the V-shaped flame. The ORZs are dominating the flow field on the sides in cases 3 and 4, generating strong recirculation zones.

To visualize the flow field in 3D, Fig. 7 shows the pathlines in 3D. The precessing vortex core can be identified in each case. Both fuels show less intense ORZ in case 1, while it is stronger in case 2, while the occupied volume remains similar. Case WCO2 is clearly at the edge of V-shaped flame formation. Distributed flames feature significantly larger ORZ, shown in cases 3 and 4.

The vortex structures are shown in Fig. 8. The characteristic IRZ of D2 is spectacular, while amorphous ORZ structures are visible for distributed combustion.

Figure 9 shows the evaporating spray, colored by droplet size. The spray size and droplet diameters decrease significantly with the increase of the atomizing pressure. The increased axial momentum creates narrower spray, and vaporization completes inside the mixing tube for cases 3 and 4. Furthermore, the penetration length into the chamber for WCO is larger, delaying mixing and ignition.

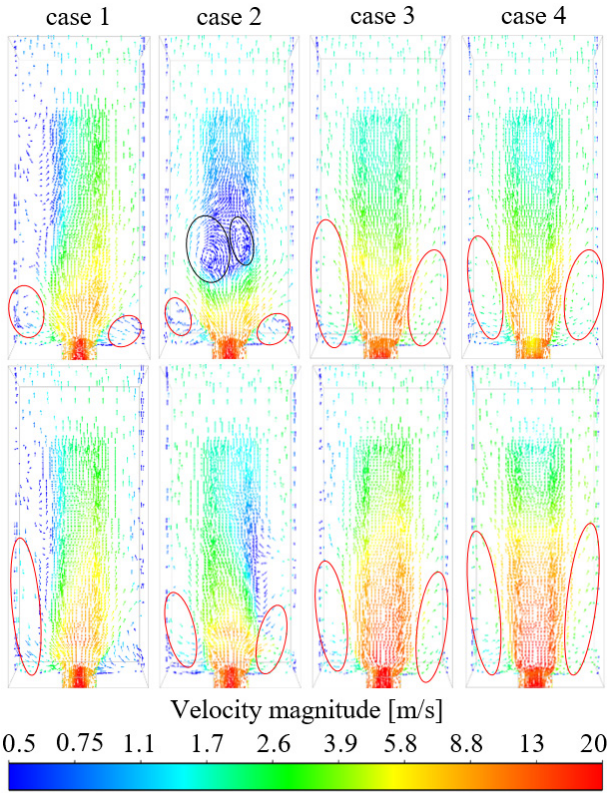

Fig. 6. Vector plot of diesel (top row) and WCO combustion (bottom row). Note the log scale.

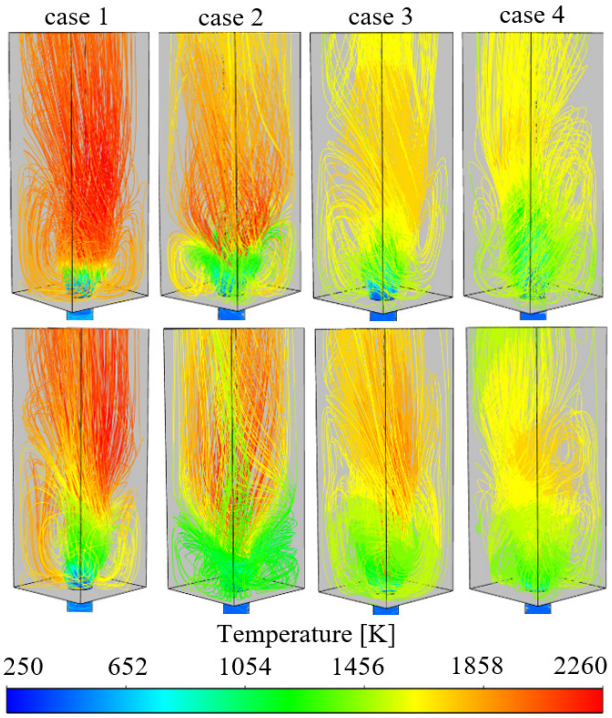

Fig. 7. Pathlines colored by temperature in the case of (top row) and WCO (bottom row) diesel combustion.

NO_x emission of WCO combustion can be seen in Table 5. The measured trend was followed by the

simulated results. Overall, the lower volatility resulted in increased emissions for WCO compared to D, however, the CFD results were the opposite.

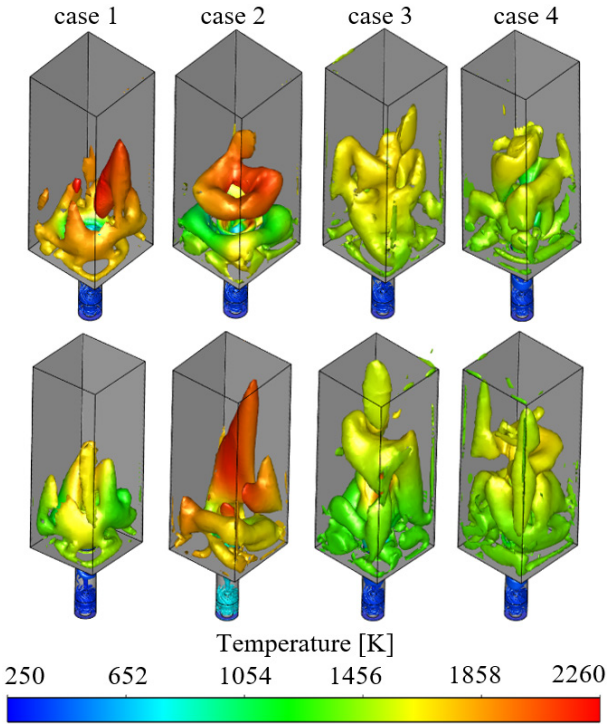

Fig. 8. Vortex structures by $\lambda_2 = -500\ 1/s^2$ colored by temperature. D (top row) and WCO combustion (bottom row).

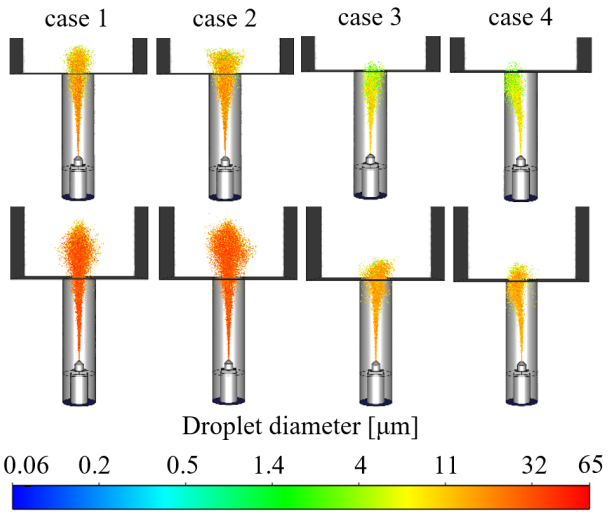

Fig. 9. Diesel (top row) and WCO (bottom row) droplet distribution colored by particle diameter. Note the log scale.

Table 5. NO_x emission on the outlet referred to 15% O_2 content in the flue gas in the case of WCO combustion.

Case	Simulated [ppm]	Measured [ppm]
1	105.4	42
2	39.8	25
3	3.6	3
4	10.7	3.5

Conclusions

Numerical analysis of diesel fuel and WCO biodiesel was presented in this study. The following conclusions were made.

The simulation of diesel fuel was successful in all cases, while the V-shaped flame of WCO combustion was missed. Note that the setup was also at the edge of the stability limit.

ORZ of distributed combustion plays a dominant role while the IRZ is absent. The shape of ORZ was highly amorphous compared to the typical flow structures of V-shaped flames. Regardless of the fuel type, the respective flames were successfully modeled.

The NO_x emission trends of the simulation were captured by the CFD analysis. However, the calculated values were significantly higher than the real ones for straight and V-shaped flames. The marginal emission of distributed flames was simulated correctly.

Acknowledgments

This work has been supported by the National Research, Development and Innovation Fund of Hungary, project №. OTKA-FK 124704 and the New National Excellence Program of the Ministry for Innovation and Technology project №. ÚNKP-20-3-II-BME-178.

References

[1] IEA. Transport: Improving the sustainability of passenger and freight transport 2020. https://www.iea.org/topics/transport (accessed February 17, 2021).

[2] Chen H-G, Zhang Y-HP. New biorefineries and sustainable agriculture: Increased food, biofuels, and ecosystem security. Renew Sustain Energy Rev 2015;47:117–32. doi:10.1016/j.rser.2015.02.048.

[3] Goh BHH, Chong CT, Ge Y, Ong HC, Ng JH, Tian B, et al. Progress in utilisation of waste cooking oil for sustainable biodiesel and biojet fuel production. Energy Convers Manag 2020;223. doi:10.1016/j.enconman.2020.113296.

[4] De Feo G, Di Domenico A, Ferrara C, Abate S, Sesti Osseo L. Evolution of Waste Cooking Oil Collection in an Area with Long-Standing Waste Management Problems. Sustainability 2020;12:8578. doi:10.3390/su12208578.

[5] Rezania S, Oryani B, Park J, Hashemi B, Yadav KK, Kwon EE, et al. Review on transesterification of non-edible sources for biodiesel production with a focus on economic aspects, fuel properties and by-product applications. Energy Convers Manag 2019;201:112155. doi:10.1016/j.enconman.2019.112155.

[6] Abdollahi Asl M, Tahvildari K, Bigdeli T. Eco-friendly synthesis of biodiesel from WCO by using electrolysis technique with graphite electrodes. Fuel 2020;270:117582. doi:https://doi.org/10.1016/j.fuel.2020.117582.

[7] Valente OS, Pasa VMD, Belchior CRP, Sodré JR. Physical–chemical properties of waste cooking oil

biodiesel and castor oil biodiesel blends. Fuel 2011;90:1700–2. doi:https://doi.org/10.1016/j.fuel.2010.10.045.
[8] Lefebvre AH, Ballal DR. Gas turbine combustion. third. Boca Raton: CRC Press; 2010. doi:10.1002/1521-3773.
[9] Xing F, Kumar A, Huang Y, Chan S, Ruan C, Gu S, et al. Flameless combustion with liquid fuel: A review focusing on fundamentals and gas turbine application. Appl Energy 2017;193:28–51. doi:10.1016/j.apenergy.2017.02.010.
[10] Karyeyen S, Feser JS, Jahoda E, Gupta AK. Development of distributed combustion index from a swirl-assisted burner. Appl Energy 2020;268:114967. doi:10.1016/j.apenergy.2020.114967.
[11] Józsa V. Mixture temperature-controlled combustion: A revolutionary concept for ultra-low NOx emission. Fuel 2021;291:120200. doi:10.1016/j.fuel.2021.120200.
[12] Zhang K, Ghobadian A, Nouri JM. Comparative study of non-premixed and partially-premixed combustion simulations in a realistic Tay model combustor. Appl Therm Eng 2017;110:910–20. doi:10.1016/j.applthermaleng.2016.08.223.
[13] Cerinski D, Vujanović M, Petranović Z, Baleta J, Samec N. Numerical analysis of fuel injection configuration on nitrogen oxides formation in a jet engine combustion chamber. Energy Convers Manag 2020;220:112862. doi:10.1016/j.enconman.2020.112862.
[14] Kuti OA, Sarathy SM, Nishida K. Spray combustion simulation study of waste cooking oil biodiesel and diesel under direct injection diesel engine conditions. Fuel 2020;267:117240. doi:10.1016/j.fuel.2020.117240.
[15] Inc. ANSYS. Ansys Fluent Theory Guide. Release 2021 R1. Canonsburg: 2021.
[16] Dixit S, Kumar A, Kumar S, Waghmare N, Thaku HC, Khan S. CFD analysis of biodiesel blends and combustion using Ansys Fluent. Mater Today Proc 2019;26:665–70. doi:10.1016/j.matpr.2019.12.362.
[17] Martin M, Holge K, editors. VDI Heat Atlas. 2nd ed. Berlin, Heidelberg: Springer-Verlag Berlin Heidelberg; 2010.
[18] Technologies L. Table of emissivity of various surfaces. Schaffhausen: Mikron Instrument Company, Inc.; 2003.
[19] Urbán A, Katona B, Malý M, Jedelský J, Józsa V. Empirical correlation for spray half cone angle in plain-jet airblast atomizers. Fuel 2020;277:118197. doi:10.1016/j.fuel.2020.118197.
[20] Savard B, Wang H, Wehrfritz A, Hawkes ER. Direct numerical simulations of rich premixed turbulent n-dodecane/air flames at diesel engine conditions. Proc Combust Inst 2019;37:4655–62. doi:https://doi.org/10.1016/j.proci.2018.08.022.
[21] Lemmon EW, McLinden MO, Friend DG. Thermophysical Properties of Fluid Systems, NIST Chemistry WebBook, NIST Standard Reference Database Number 69 n.d. doi:doi:10.18434/T4D303.
[22] Riedel L. Kritischer Koeffizient, Dichte des gesättigten Dampfes und Verdampfungswärme. Untersuchungen über eine Erweiterung des Theorems der übereinstimmenden Zustände. Teil III. Chemie Ing Tech 1954;26:679–83. doi:10.1002/cite.330261208.
[23] Elbro HS, Fredenslund A, Rasmussen P. Group contribution method for the prediction of liquid densities as a function of temperature for solvents, oligomers, and polymers. Ind Eng Chem Res 1991;30:2576–82. doi:10.1021/ie00060a011.
[24] Ruzicka V, Domalski E. Estimation of the Heat Capacities of Organic Liquids as a Function of Temperature Using Group Additivity II.: Compounds of Carbon, Hydrogen, Halogens, Nitrogen, Oxygen, and Sulfur. J Phys Chem Ref Data 1993;22:619–57.
[25] Ramírez Verduzco LF. Density and viscosity of biodiesel as a function of temperature: Empirical models. Renew Sustain Energy Rev 2013;19:652–65. doi:https://doi.org/10.1016/j.rser.2012.11.022.
[26] Brock JR, Bird RB. Surface tension and the principle of corresponding states. AIChE J 1955;1:174–7. doi:https://doi.org/10.1002/aic.690010208.
[27] Joback KG. A Unified Approach to Physical Property Estimation Using Multivariate Statistical Techniques. Massachusetts Institute of Technology, Department of Chemical Engineering; 1984.
[28] Joback KG, Reid RC. Estimation of pure-component properties from goup-contributions. Chem Eng Commun 1987;57:233–43. doi:10.1080/00986448708960487.
[29] Lucas K. Die Druckabhängigkeit der Viskosität von Flüssigkeiten – eine einfache Abschätzung. Chemie Ing Tech 1981;53:959–60. doi:10.1002/cite.330531209.
[30] Svehla RA. Estimated Viscosities and Thermal Conductivities of Gases at High Temperatures. Cleveland, Ohio: NASA Tech. Rept. R-132, Lewis Research Center; 1962.
[31] Fuller EN, Schettler PD, Giddings JC. New method for prediction of binary gas-phase diffusion coefficients. Ind Eng Chem 1966;58:18–27. doi:10.1021/ie50677a007.
[32] Fuller EN, Ensley K, Giddings JC. Diffusion of halogenated hydrocarbons in helium. The effect of structure on collision cross sections. J Phys Chem 1969;73:3679–85. doi:10.1021/j100845a020.
[33] Yaws CL. The Yaws Handbook of Vapor Pressure. Oxford: Gulf Professional Publishing; 2015. doi:10.1016/c2014-0-03590-3.